

Non-equilibrium plasma distribution in the wake of a slender blunted-nose cone in hypersonic flight and its effect on the radar cross section

Original

Non-equilibrium plasma distribution in the wake of a slender blunted-nose cone in hypersonic flight and its effect on the radar cross section / Esposito, S.; Scarabosio, A.; Vecchi, G.; D'Ambrosio, D.. - In: AEROSPACE SCIENCE AND TECHNOLOGY. - ISSN 1270-9638. - STAMPA. - 155:Part 3(2024). [10.1016/j.ast.2024.109699]

Availability:

This version is available at: 11583/2994356 since: 2024-11-13T00:31:49Z

Publisher:

Elsevier

Published

DOI:10.1016/j.ast.2024.109699

Terms of use:

This article is made available under terms and conditions as specified in the corresponding bibliographic description in the repository

Publisher copyright

(Article begins on next page)



Non-equilibrium plasma distribution in the wake of a slender blunted-nose cone in hypersonic flight and its effect on the radar cross section

Salvatore Esposito^{a,*}, Andrea Scarabosio^b, Giuseppe Vecchi^a, Domenic D'Ambrosio^c

^a Department of Electronics and Telecommunications, Politecnico di Torino, Corso Duca degli Abruzzi, 24, Torino, 10129, Italy

^b LINKS Foundation, Via Pier Carlo Boggio, 61, Torino, 10138, Italy

^c Department of Mechanical and Aerospace Engineering, Politecnico di Torino, Corso Duca degli Abruzzi, 24, Torino, 10129, Italy

ARTICLE INFO

Communicated by Damiano Casalino

ABSTRACT

This paper presents numerical results in hypersonic aerothermodynamics, a critical field within aerospace engineering, traditionally focusing on reentry capsules and more recently, slender hypersonic vehicles. While capsules typically undergo near-field analysis to assess heat flux and pressure distributions for Thermal Protection System sizing, slender bodies demand additional attention to wake dynamics due to plasma presence. Plasma can significantly affect the Radar Cross Section (RCS) of these vehicles, which require tracking during flight due to their maneuvering and sustained flight capability.

Utilizing Computational Fluid Dynamics tools, we explore plasma distribution around a slender blunted cone, considering altitudes and Mach number regimes that may characterize gliding or sustained atmospheric hypersonic flight, emphasizing its impact on RCS. Our study integrates an aerothermodynamic model incorporating non-equilibrium relaxation equations for gas composition and energy. By evaluating characteristic plasma quantities, we underscore the importance of wake plasma for subsequent electromagnetic wave analysis, crucial for understanding RCS. Furthermore, we highlight the necessity for collaborative efforts between Computational Fluid Dynamics (CFD) and Computational Electro-Magnetics (CEM) disciplines to address this challenging interdisciplinary problem.

1. Introduction

Hypersonic flight, defined as the regime where the Mach number exceeds 5, is characterized by distinct physical phenomena within the flow field. At hypervelocity, an object creates a detached shockwave, leading to intense compression and heating of the air. The resulting high temperatures prompt internal energy redistribution through vibrational and electronic modes, alongside chemical reactions like dissociation, exchange, and ionization within the flow field [1]. If temperature and pressure conditions permit ionization, which typically occurs near the nose of the vehicle, charged particles form and are convectively transported along the body into the trailing wake. This plasma envelope significantly influences electromagnetic (EM) wave propagation, impacting radio communications and the radar signature of the aircraft [2–5].

The above mentioned high-temperature phenomena occur with characteristic time scales similar to those of fluid flow, leading to thermochemical non-equilibrium that significantly influences aerodynamic

forces and heat exchanges [6–8]. Multi-temperature models are widely used to describe the non-equilibrium of reacting gas flows [9].

In aerospace engineering, thermochemical models are essential for hypersonic aerothermodynamics analysis, especially when examining the flow field around reentry vehicles, typically characterized by blunt bodies such as capsules. However, recent advancements have led to the design of slender hypersonic vehicles that operate within the Earth's atmosphere. Although these vehicles still feature blunted noses and leading edges to minimize convective heat fluxes at the forward parts of the vehicle, they aim to mitigate wave drag associated with shock waves [10,11].

Most of the existing literature about hypersonic aerothermodynamics concentrates on predicting heat flux and pressure distributions on the vehicle's surface for designing thermal protection systems, evaluating aerodynamic coefficients, or assessing stability properties. The literature on the subject is wide and it would be impossible to list all the pertinent publications. In the following, we will mention a few papers in the awareness that these are just a few samples. For example, [Carandente](#)

* Corresponding author.

E-mail address: salvatore_esposito@polito.it (S. Esposito).

Nomenclature

A	frequency factor [$m^3 \cdot kmol^{-1} \cdot s^{-1} \cdot K^{-N_T}$]	k_f	forward reaction rate constant [$m^3 \cdot kmol^{-1} \cdot s^{-1}$]
E_a	activation energy [$J \cdot kmol^{-1}$]	m_e	electron mass [kg]
K_b	Boltzmann constant [$J \cdot K^{-1}$]	n	number density [m^{-3}]
K_c	equilibrium constant [$kmol^\alpha \cdot m^{-3\alpha}$] α depending on the order of reaction	n_e	electron number density [m^{-3}]
N_T	temperature exponent	t	time [s]
R	universal gas constant [$J \cdot kmol^{-1} \cdot K^{-1}$]	\mathbf{r}	position vector [m]
T	roto-translational temperature [K]	ϵ_0	vacuum permittivity [$F \cdot m^{-1}$]
T_b	backward temperature [K]	ϵ_r	relative dielectric constant
T_e	electron temperature [K]	ν_c	neutral-plasma angular collision frequency ... [$rad \cdot s^{-1}$]
T_f	forward temperature [K]	$\sigma_{i,e}$	cross-section for neutral-electron scattering of the neutral species i [m^2]
$T_{v,e}$	vibrational-electron temperature [K]	ω	angular frequency [$rad \cdot s^{-1}$]
e	electron charge [C]	ω_p	angular plasma frequency [$rad \cdot s^{-1}$]
i	imaginary unit		

et al. [12] analyzed aerothermodynamic loads to assess the longitudinal stability of a sphere-cone configuration with varying half-cone angles. Kumar and Mahulikar [13] investigated the aerothermal characteristics of a hypersonic lifting body vehicle considering two different sweepback angles. Additionally, Zuppari et al. [14] provided a study on aerothermodynamic loads and longitudinal stability of a deployable capsule, offering insights into the plasma sheet during the trajectory. Schettino et al. [15] proposed an aerodynamic characterization of a hypersonic glider by providing an aerodynamic database to be used for flight trajectory assessment and the design of various subsystems.

Further analyses explore the radio blackout and electromagnetic (EM) scattering during atmospheric descent due to the plasma sheath around reentry vehicles, adopting aerothermodynamic models embedded in CFD simulations to predict the plasma characteristics. Mather et al. [16] describe how design and mission variables influence plasma characteristics and their impact on signal attenuation, which may degrade onboard communication system performance. Ramjatan et al. [17] propose a CFD study on a blunt-nosed cone under various flight conditions to predict communication blackout periods and assist in designing an alert transmitter. Takahashi et al. [18] investigated plasma attenuation and radio frequency blackout of a reentry vehicle in the atmosphere. Cong et al. [19] studied the impact of plasma sheath on the EM scattering of a blunt cone. Scarabosio et al. [20] used a ray tracing asymptotic method to evaluate the EM wave radiation and scattering for the IXV reentry vehicle considering the plasma distribution also into the wake of the aircraft.

In slender bodies with blunted noses, plasma formation is typically confined to the nose, with charged particles then transported downstream along the vehicle, persisting within the wake. In this context, non-equilibrium relaxation is pivotal for assessing the presence of plasma around the vehicle (plasma sheath) and in the wake. Extensive research on this subject is still in its infancy, given that the prediction of the RCS of slender hypersonic vehicles is a relatively new, multi-disciplinary problem requiring collaboration between Computational Fluid Dynamics (CFD) and Computational Electromagnetics (CEM). The latter receives the numerical results obtained by the former, which are then used to characterize the collisional and inhomogeneous plasma media through which electromagnetic waves propagate.

While the open literature contains numerous research articles analyzing interactions between plasma and electromagnetic wave propagation in hypersonic flight, manuscripts specifically targeting the effect of a long wake using accurate non-equilibrium models and not in reentry conditions are very rare. To the best of the authors' knowledge, this has only been attempted by Qian et al. [21], from whom we adopted the geometrical configuration, and Tong et al. [22]. The aerodynamic configuration considered in [21] consists of a blunted cone simulated in the hypersonic regime at altitudes of 30, 50, and 70 km, with Mach

numbers of 7, 8, and 10. The angle of attack is normally zero, but for the combination of Mach 10 and 50 km altitude, attitudes of 5, 10, and 15 degrees are also considered. The authors declare the adoption of a 7-species chemical non-equilibrium model and include a single-temperature vibrational-electronic non-equilibrium model. In [22], the authors considered a blunted cone and included a very long wake, approximately 67 times the body length, in the computational domain. They conducted their simulation at a 48 km altitude with freestream conditions of Mach 6, 9, and 13. At Mach 13, they also present results at angles of attack of 5 and 10 degrees. The governing equations adopted are the compressible Navier-Stokes equations, including a 7-species thermochemical and vibrational-electronic non-equilibrium model. The calculated flowfield and plasma distribution are utilized to investigate the excitation and power spectrum characteristics of electromagnetic radiation for the plasma wake, with the aim of proposing a new method for detecting reentry targets through the excited electromagnetic radiation phenomenon.

Many authors considered the RAM-C-II geometry. RAM-C-II is a flight experiment carried out in the sixties to investigate the telecommunication blackout phenomenon [23]. For instance, Sha et al. [24] simulated the flow field around the RAM-C-II vehicle at 61 and 71 km altitude and speed 7650 m/s, resulting in freestream Mach numbers equal to 23.9 and 24.9, respectively. They calculated the flowfield by solving the Navier-Stokes equations in the axial symmetry approximation and adopted thermo-chemical models similar to those considered in this paper, namely a 7 species model including NO^+ and e^- . Apart from classical dissociation and exchange reactions, they considered a single electron-impact ionization reaction for NO^+ and included vibrational-electronic non-equilibrium in their model. They assumed a fixed temperature wall set at 1500 K. The wake behind the blunted cone is about 3.5 times the vehicle length. This type of modeling and geometry closely resembles that considered in this paper, but the high Mach number conditions related to the RAM-C-II experiment constitute a major difference. The same difference is found in the paper by Niu et al. [25]. The latter study the hypersonic flow about a blunted cone (RAM-C-like configuration). They do not explicitly define the fluid model nor the thermochemical model they adopt, but they mention that they obtained the flowfield data from reference [26], a book written in Chinese. In the chapter they mention in their reference, it seems that the Burnett equations, including thermochemical non-equilibrium effects, are considered. The authors focus on four flight configurations, at altitudes of 40, 50, 60 and 70 km, Mach number ranging from 23 to 24, and a few angles of attack. They do not consider the vehicle wake and they mostly focus on the backward polarization scattering characteristics of the plasma-sheath-covered vehicle. Bian et al. [27–29] also consider the RAM-C-II geometry. In their research articles, they focus on methods for analyzing the EM scattering characteristics of hypersonic

vehicles surrounded by a plasma sheath. They utilized the aerothermodynamic flowfield published in [30], another book written in Chinese that contains CFD results on various geometries, including the RAM-C-II. The book includes numerical results obtained at altitudes between 30 to 70 km (in 5 km steps), Mach numbers of 15, 20, and 25, and a zero angle of attack. The wake behind the vehicle is simulated up to a distance of approximately one and a half vehicle lengths. Reference [30] provides data on pressure, temperature, and electron number density on selected planes. The thermochemical models adopted include a 7-species chemical non-equilibrium and single-temperature vibrational-electronic relaxation. Similarly, Zhang et al. [31] consider the RAM-C-II geometry at 40, 50, and 60 km altitude and Mach 15. They also adopt a 7 species chemical non-equilibrium model and incorporate vibrational non-equilibrium. However, they do not focus on the wake, which is just one body length long, but are rather interested in the effect of the plasma sheath around the vehicle and address the second part of their paper to the effect of wall roughness. On the other hand, Wang et al. [32] considered a blunted cone at 60 km altitude and Mach numbers between 10 to 14. They incorporated a wake approximately three times the body length in their simulations, but they seemingly used the Euler equations without any embedded thermochemical model to assess temperature and pressure fields, from which they estimated density in the wake and plasma distribution around the vehicle using semi-empirical formulas. Shao et al. [33] investigated an HTV-2 type vehicle at 75 km altitude, Mach 26, and zero angle of attack. In their simulations, they did not include the wake. Additionally, they augmented the classical 7-species non-equilibrium thermochemical model, which incorporates single-temperature vibrational energy relaxation, with the effect of non-ionizing ablation products.

Although previous studies have examined the aforementioned aspects individually, to the best of the authors' knowledge, this work is the first to integrate an analysis of non-equilibrium plasma in the wake of a slender body over a wide range of Mach numbers and altitudes that are distinct from reentry conditions. Such an approach provides a comprehensive understanding of plasma dynamics specific to slender hypersonic vehicles, with significant implications for electromagnetic wave propagation.

To this purpose, this paper presents a comprehensive numerical analysis of the plasma field around and in the wake of a slender body, under hypersonic and sub-orbital flight conditions at different altitudes and Mach numbers, utilizing Computational Fluid Dynamics tools to examine its impact on the Radar Cross Section. The study delves into key thermochemical phenomena, such as dissociation, ionization, chemical and energy relaxation, and also offers a comparison of two thermochemical models. The aerothermodynamic models incorporate a one-temperature non-equilibrium relaxation equation for aggregate vibrational-electronic energy and non-equilibrium relaxation equations for gas composition, including ionized species and electrons. In particular, the air-gas mixture is assumed to comprise seven species, including NO^+ ions and electrons. It covers a broad range of flight conditions, with altitudes ranging from 20 to 70 km and Mach numbers between 10 and 16, which are more related to gliding or sustained flight within the atmosphere than to typical Earth reentries. For each condition, we provide detailed measurements of rotational-translational and vibrational-electronic temperatures, electron number density, and electromagnetic properties of the plasma, including plasma frequency, collision frequency, and dielectric constant, with a primary focus on the wake region. Additionally, we investigate a scenario with a non-zero angle of attack, highlighting how the incidence angle affects electron density and plasma characteristics in the wake.

To further emphasize the significance of our findings, we conduct a quantitative analysis employing Computational Electromagnetics adopting a full-wave approach. This investigation delves into the effects of wake plasma on radar cross-section, shedding light on how the plasma influences the radar signature of hypersonic vehicles.

2. Theoretical and numerical methods

2.1. Thermochemical models

With the assumption of a continuous flow, air is described using the Navier-Stokes equations for a compressible, viscous, and chemically reacting mixture of gases. At hypervelocity, the model must also account for physical phenomena such as dissociation, ionization, and vibrational and electronic energy relaxation. In this regard, air is viewed as a mixture comprising seven species, namely, mono-atomic oxygen (O), mono-atomic nitrogen (N), nitrogen oxide (NO), diatomic oxygen (O_2), diatomic nitrogen (N_2), positive ions (NO^+), and electrons (e^-). Park's two-temperature model is employed for characterizing non-equilibrium phenomena [34]. This model combines translational and rotational energy modes into a single equilibrium temperature (roto-translational temperature) while accounting for vibrational and electronic modes through a single non-equilibrium temperature. The two-temperature model is effective in capturing thermochemical non-equilibrium processes in high-temperature gases, as well as accurately depicting radiation overshoot downstream of a strong shockwave [34,35]. The two-temperature model is commonly employed to describe the thermal and chemical non-equilibrium state of gaseous species in the atmosphere [34,36,37].

The thermodynamic and diffusion properties of each species were determined from the fittings presented in [38]. The forward rate constants are described by an Arrhenius-type relation:

$$k_{f,k} = A_k T^{N_T} e^{\frac{E_{a,k}}{RT}} \quad (1)$$

In equation (1), A_k represents the frequency factor of reaction k , $E_{a,k}$ is the activation energy, and N_T is the temperature exponent. These parameters are determined using the thermochemical model proposed in [39,40]. The backward reaction rates are determined using the equilibrium condition and can be expressed as:

$$k_{b,k} = \frac{k_{f,k}(T_b)}{K_c(T)} \quad (2)$$

The equilibrium constants denoted as K_c , are calculated using the Gibbs free energies, as explained in [1]. The backward and forward rate constants are determined using temperatures, denoted as T_f and T_b , respectively, which depend on the energy states of the reacting species. These temperatures can be either the translational-rotational temperature T , the vibrational-electronic temperature $T_{v,e}$, or a combination of the two. Specific details about T_f and T_b are shown in Table 1. Recent shock tube experiments have revealed discrepancies in the kinetic parameters of the Park model [41]. Chemical kinetics parameters established in the early 1990s were primarily applicable to temperature ranges up to 5000 K, leading to inaccuracies. Addressing these challenges, Kim and Jo's recent research integrates more precise and contemporary studies, leveraging ab initio calculated potential energy surfaces and comparing results with shock tube experiments conducted at significantly higher translational temperatures. In our analysis, we also incorporate forward rate constants for dissociation reactions derived from Kim and Jo's recent studies [41]. This allows for a comparison between the results we have obtained from Park's kinetic model [39,40], and those obtained by adopting the more recent model provided by Kim and Jo. In Table 1, the Arrhenius coefficients that differ between the Park and the Kim and Jo models are highlighted in bold font.

2.2. Electromagnetic plasma model

Another objective of this study is to use the characteristics of the plasma field from CFD to calculate the scattering of radio frequency waves. In fact, the plasma itself, as inhomogeneous dielectric, influences the propagation and scattering of EM radiation in various ways: through refraction, reflection and absorption. The study considers that while the medium remains stationary, the EM fields exhibit a time variation expressed by $e^{i\omega t}$. The primary focus of the research is on the frequency

Table 1
Kinetic parameters.

Reactions	Third body	A Kim et al.	A Park et al.	N _T Kim et al.	N _T Park et al.	T _f	T _b
Dissociation reactions							
N ₂ + M ⇌ N + N + M	e ⁻	3.0 e21	3.0 e21	-1.6	-1.6	$\sqrt{TT_{v,e}}$	T
	NO ⁺	7.0 e18	7.0 e18	-1.6	-1.6	"	"
	NO	7.0 e18	7.0 e18	-1.6	-1.6	"	"
	N	3.591 e17	3.0 e19	-1.226	-1.6	"	"
	O	3.0 e19	3.0 e19	-1.6	-1.6	"	"
	O ₂	7.0 e18	7.0 e18	-1.6	-1.6	"	"
	N ₂	1.216 e17	7.0 e18	-1.214	-1.6	"	"
O ₂ + M ⇌ O + O + M	NO ⁺	3.354 e12	2.0 e18	-0.2726	-1.5	"	"
	NO	3.354 e12	2.0 e18	-0.2726	-1.5	"	"
	N	1.0 e19	1.0 e19	-1.5	-1.5	"	"
	O	3.0 e18	1.0 e19	-1.5	-1.5	"	"
	O ₂	1.117 e22	2.0 e18	-2.585	-1.5	"	"
	N ₂	3.354 e12	2.0 e18	-0.2726	-1.5	"	"
NO + M ⇌ N + O + M	NO ⁺	9.964 e11	5.0 e12	0.0	0.0	"	"
	NO	9.964 e11	1.1 e14	0.0	0.0	"	"
	N	9.964 e11	1.1 e14	0.0	0.0	"	"
	O	9.964 e11	1.1 e14	0.0	0.0	"	"
	O ₂	1.50 e12	5.0 e12	0.0	0.0	"	"
	N ₂	1.50 e12	5.0 e12	0.0	0.0	"	"
Exchange reactions							
NO + O ⇌ N + O ₂		8.4 e9	8.4 e9	0.0	0.0	T	T
N ₂ + O ⇌ NO + N		5.7 e9	5.7 e9	0.42	0.42	"	"
Associative ionization reactions							
N + O ⇌ NO ⁺ + e ⁻		5.3 e9	5.3 e9	0.0	0.0	T	$\sqrt{TT_{v,e}}$

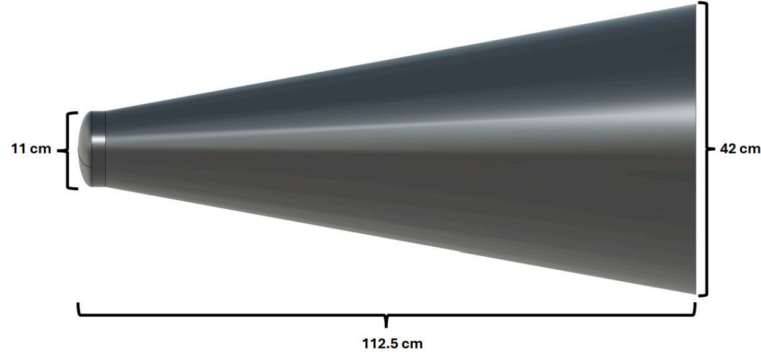


Fig. 1. Body geometry.

ranges where the plasma response is mainly influenced by the motion of electrons whilst assuming “cold” (stationary) ions. We can disregard temperature effects and higher-order collective kinetic effects, provided that the phase velocity of the wave is significantly greater than the thermal velocity of the plasma, but we retain the effects of collisions and neutral species in the plasma.

To model this behavior, we employ an EM cold plasma framework [2], which treats the medium as inhomogeneous, unmagnetized, and collisional. This approach aligns with those used in previous studies, such as [42], and simplifies the constitutive relations, effectively reducing the model to the well-known Drude model [43]:

$$\epsilon_r(\mathbf{r}) = 1 - \frac{\omega_p^2(\mathbf{r})}{\omega(\omega - i\nu_c(\mathbf{r}))} = 1 - \frac{\omega_p^2(\mathbf{r})}{(\omega^2 + \nu_c^2(\mathbf{r}))} + i \frac{\omega_p^2(\mathbf{r})\nu_c}{\omega(\omega^2 + \nu_c^2(\mathbf{r}))} \quad (3)$$

where \mathbf{r} is the position vector, ω is the angular frequency of the EM wave and the angular plasma frequency, ω_p , is defined by the following equation:

$$\omega_p(\mathbf{r}) = \sqrt{\frac{n_e(\mathbf{r})e^2}{m_e\epsilon_0}} \quad (4)$$

In Eq. (4), n_e denotes the density of electrons, e stands for the charge of an electron, m_e denotes the mass of an electron, and ϵ_0 represents the permittivity of vacuum. The neutral-plasma angular collision frequency is determined by the following formula [44]:

$$\nu_c(\mathbf{r}) = \sum_{i=1}^N n_i(\mathbf{r})\sigma_{i,e}(T_e) \sqrt{\frac{8K_b T_e(\mathbf{r})}{\pi m_e}} \quad (5)$$

where T_e denotes the temperature of electrons, specifically referring to the vibrational-electron temperature within our model. Meanwhile, n_i represents the number density of the i -th neutral species, and $\sigma_{i,e}$ signifies the cross-section for neutral-electron scattering of the neutral species i . Finally, K_b stands for the Boltzmann constant. The neutral-electron cross-sections are taken from [38]. Considering Eq. (3), when the electron number density is sufficiently high and the plasma frequency matches or exceeds the EM wave frequency, the real component of the permittivity can become null or negative (for sufficiently small collision frequencies). This causes the traveling EM wave to turn into an evanescent state, which rapidly loses intensity as it passes through the affected region of space. In such situations, the plasma surface replaces the surface of objects, causing reflection and distortion of radar signals. Even if the plasma frequency doesn't reach the cut-off thresholds ($\text{Re}\{\epsilon_r\} = 0$), refraction phenomena can still occur if the real part of the dielectric constant is smaller than one, leading to EM wave re-distribution and reduced re-radiation. The propagation of the wave is determined by the real part of the permittivity, while the imaginary component is responsible for collisional absorption. In this absorption mechanism, energy is transferred from electrons energized by EM waves to neutral particles.

2.3. Numerical model

The slender cone under study, presented in Fig. 1, measures 1.125 meters in length and features an ellipsoid nose with a major radius of 5.5 cm and a minor radius of 2.5 cm. This is followed by a cylindrical

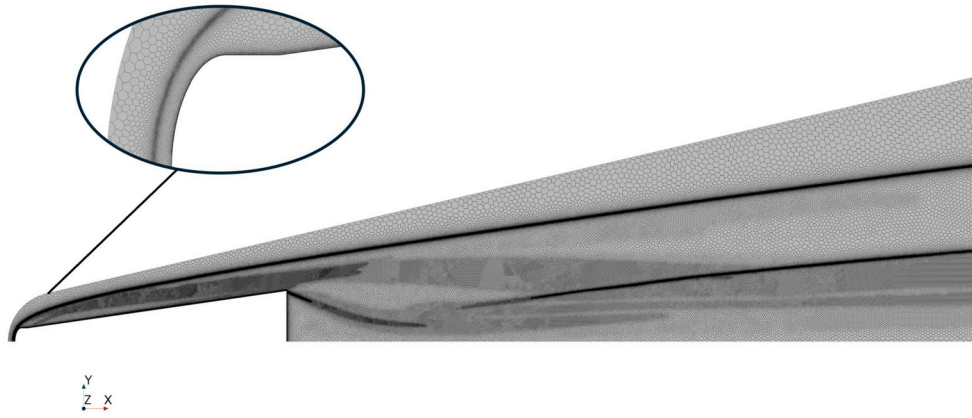


Fig. 2. Refined grid at an altitude of 30 km and a Mach number of 14.

segment that spans 2.5 cm, and a cone with a semi-opening angle of 8.2047° , as described in [21]. This geometric arrangement serves as a good foundation for modeling plasma generation during hypersonic atmospheric flight around a thin body.

The computational domain extends 2.875 m beyond the rear of the body to capture plasma behavior in the wake. While charged particles are predominantly generated at the nose and carried downstream by convection, their concentration decreases along the axis unless strong ionization occurs due to shock interactions. Under certain flight conditions, intense reattachment shocks can lead to additional electron generation in the early wake. Extending the domain further would significantly increase computational costs without yielding substantial new insights into the far wake region.

The bow shock leads to increased temperatures and flow compression, particularly in the nose region where the most of thermochemical activity occurs. In order to accurately capture this area, we use adaptive mesh refinement. The mesh is refined based on the magnitude of the Mach number gradient. An example of a specific flight condition is shown in Fig. 2. Refined grids have a maximum number of cells ranging from 300,000 to 500,000 for axisymmetric cases, and up to approximately 39 million for a 3D case with a non-zero angle of attack. Three refinements are performed for each simulation, with the order of the minimum cell size of 10^{-5} m at the wall and 10^{-4} m in the shock region. Regarding the 3D simulation, the wake has been refined independently of the Mach number gradient, with a cell size of 2 cm. This size ensures a sufficiently detailed description of the wake phenomena using a second-order accuracy scheme for the inviscid terms while keeping the number of points contained.

The CFD simulations were performed using CFD++.19.1, a commercial software solver suitable for simulating both compressible and incompressible fluid flow [45]. It features a second-order Total Variation Diminishing (TVD) limited discretization scheme built upon a multi-dimensional interpolation framework. A HLLC Riemann solver was employed to compute the inviscid fluxes [46]. The simulations were steady Reynolds-averaged Navier-Stokes (RANS) simulations utilizing a SST $k - \omega$ turbulence model [47] except for the 70 km altitude where a laminar flow condition has been applied. It is worthwhile noting that adopting a RANS model doesn't account for all possible phenomena associated with a turbulent wake, particularly those related to its intrinsic locally unsteady nature. For example, early analysis of the radar signature in the Trailblazer flying experiments [48,49] seemed to indicate a random or noisy character of the signal, which was attributed to an increased scattering from an ionized turbulent region. Despite this, using a RANS model, is a reasonable trade-off between accuracy and calculation time, as the multiple scaled nature of the flowfield around slender bodies with blunted leading edges in hypersonic flight is already demanding in terms of mesh resolution. Reaching the mesh size required for DES or LES simulations, not to mention DNS, in a very long wake would be

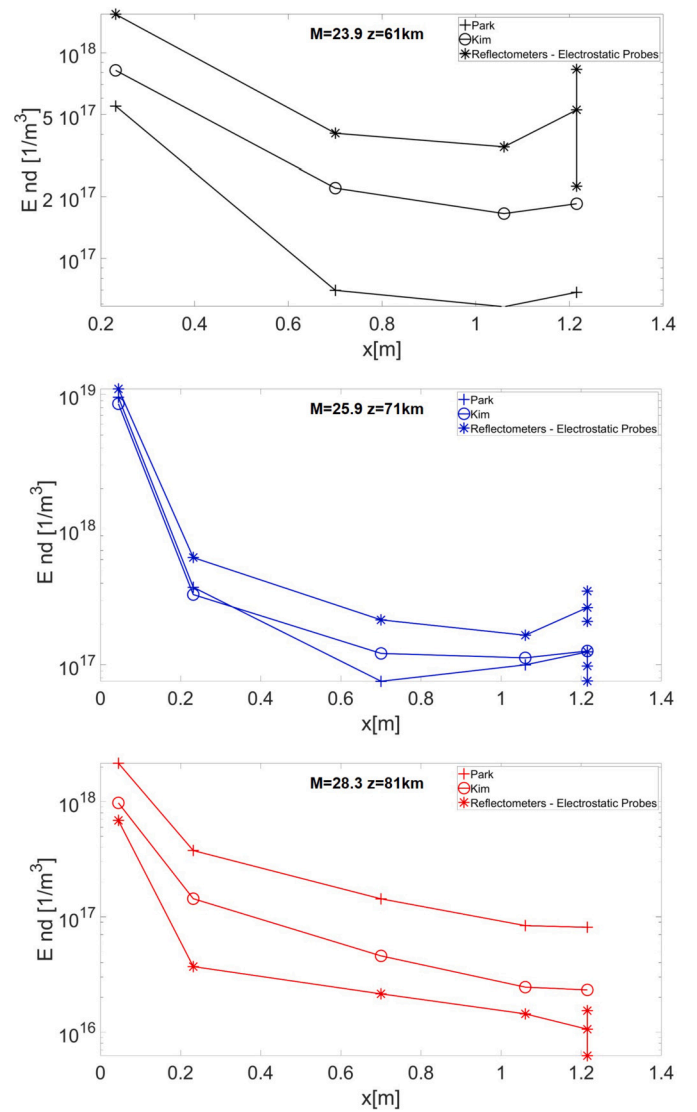


Fig. 3. Comparison of numerical results of the electron number density with experimental data for the RAM C-II case [23] considering two thermochemical models. Error bars are provided only for the results at about $x = 1.2$ m and they refer to the electrostatic rake measurements.

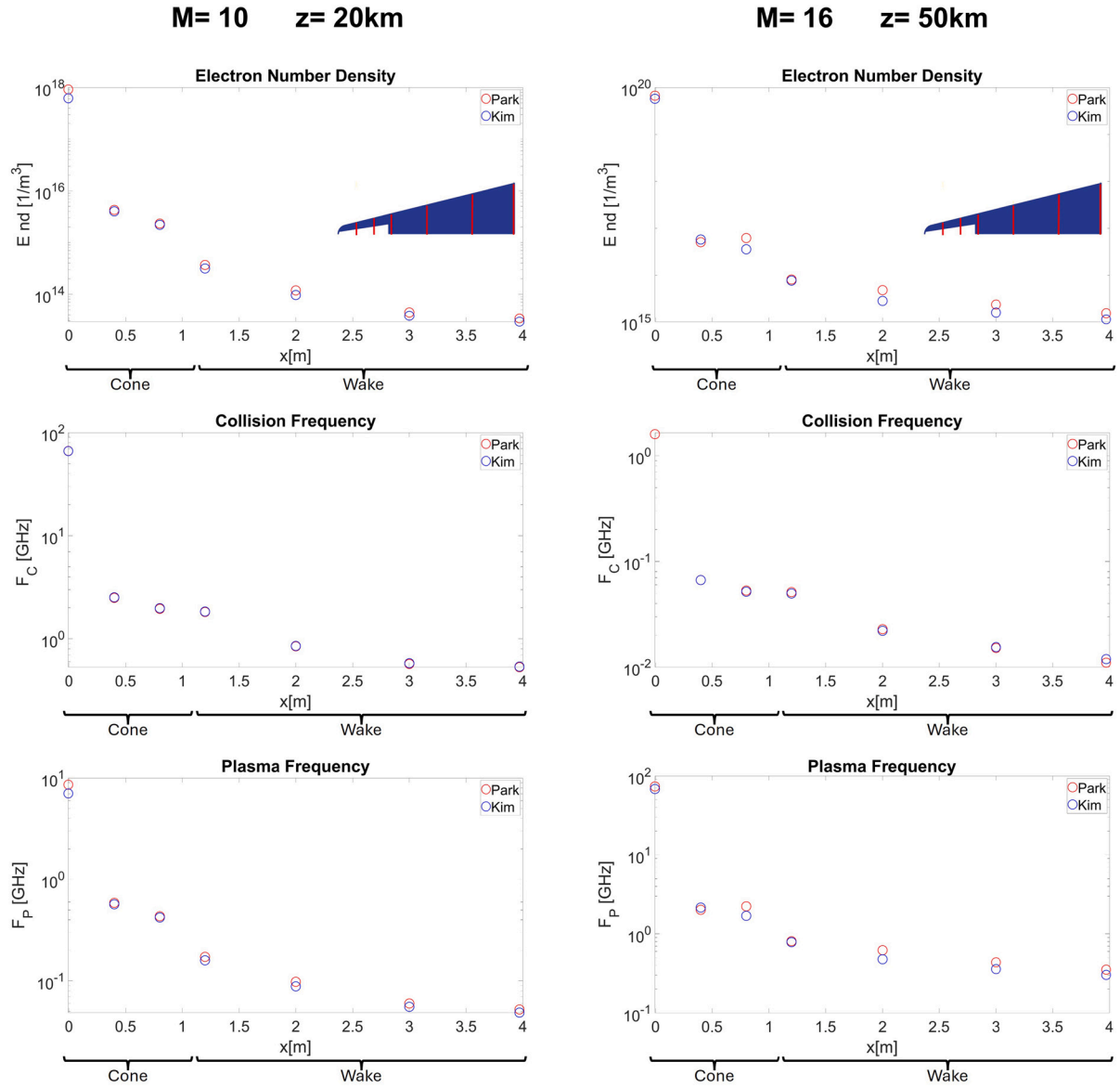


Fig. 4. Maxima electron number density, collision frequency, and plasma frequency along the stagnation axis and at various stations (red lines in the inset). (For interpretation of the colors in the figure(s), the reader is referred to the web version of this article.)

prohibitively demanding for normally accessible HPC resources. Nevertheless, the effect of local unsteadiness in a turbulent plasma wake certainly deserves further investigation.

The CFD analyses were conducted under various flight conditions, encompassing Mach numbers ranging from 10 to 16 and altitudes from 20 to 70 km, while maintaining non-catalytic walls and employing a radiation-adiabatic boundary condition. In this context, the radiation-adiabatic wall boundary condition signifies that the wall behaves as adiabatic, yet it can emit the heat it receives from the flow. This condition operates under the assumption that the gas is transparent to radiation moving away from the wall, while the wall undergoes radiative cooling. Previous studies have demonstrated that, in many instances, this condition yields reasonably accurate surface temperature estimates compared to actual flight data [50]. For the current study, a surface emissivity of 0.8 is assumed.

3. Results

The following are the results of our CFD analyses for the analyzed flight conditions. Due to the complex nature of hypersonic flow fields,

we will validate the thermochemical models described in the previous section and compare the results for two different scenarios in atmospheric hypersonic flights. Finally, we will present the results of CEM analysis to evaluate the impact of plasma (both around the body and in the wake) on the radar signature of the cone.

3.1. Validation and comparison of thermochemical models

We initially aimed to compare our study results against those presented by Qian et al. [21], particularly focusing on electron number density. Our interest in comparing with Qian et al. stems from their analysis of a slender body with a significant wake in hypersonic atmospheric flight rather than a conventional re-entry case.

However, notable disparities emerged when scrutinizing electron number density values derived from our thermochemical models in comparison to theirs, specifically at a scenario featuring a Mach number of 8 and an altitude of 30 km. Unfortunately, the lack of information on the kinetic parameters utilized in their study hindered a thorough comparison. Consequently, validating our thermochemical models by comparing them with those available for the RAM C-II case [23] seemed

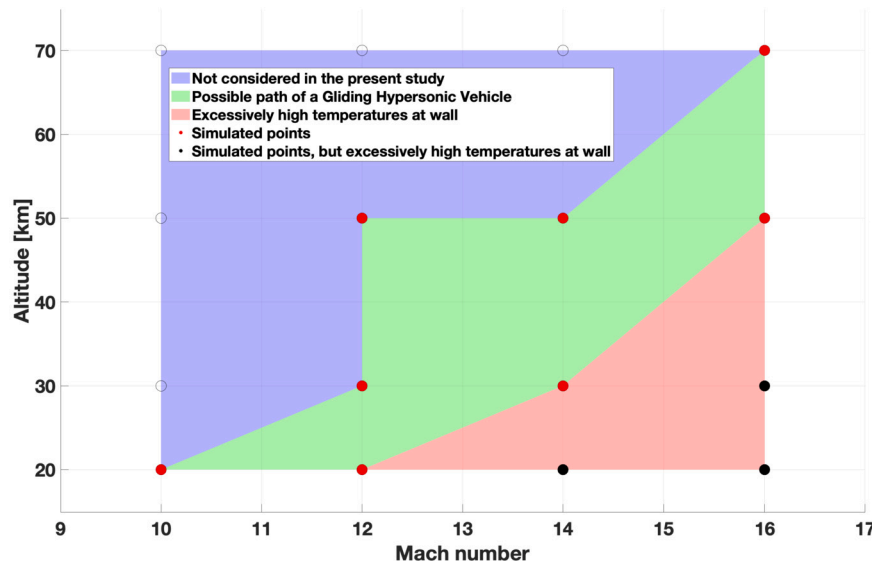


Fig. 5. Map of the simulated trajectory points.

more feasible. The experimental data are based on the maximum electron density values measured via reflectometers and electrostatic probes placed along the aircraft's body. The analysis of three different flight conditions in Fig. 3 shows that both models are consistent in the trends of electron densities compared to experimental results. It is noteworthy that the results from both Kim and Park's models tend to overestimate electron density at 81 km altitude while underestimating it at 61 km altitude. Conversely, at 71 km altitude, the results from both models demonstrate relatively consistent magnitudes, with deviations from experimental data being less pronounced.

The application of Kim and Jo's latest model yields results that demonstrate a greater consistency with experimental data when compared to those produced by Park's model. However, it's important to note that while Kim's results seem more favorable, they are evaluated against experimental data often characterized by considerable uncertainties, particularly under hypersonic flight conditions. Additionally, it is crucial to recognize that thermochemical models rely on kinetic parameters derived from experiments conducted at significantly lower temperatures than those encountered during hypersonic flight, which are responsible for plasma formation. This discrepancy introduces inherent uncertainties into the models, as the experimental conditions may not accurately represent the thermochemical behavior at the elevated temperatures present in real flight scenarios. Although these models currently provide the best approach for describing high-temperature non-equilibrium thermochemical processes, the aforementioned limitations should be acknowledged when interpreting the results, especially considering the discrepancies observed in the experimental data from the RAM-C II case.

Additionally, these findings apply to a standard atmospheric re-entry scenario, characterized by highly rarefied air and significantly high Mach numbers. In order to conduct a thorough comparison between the models adopted, we have analyzed scenarios that closely resemble hypersonic flight in the Earth's atmosphere. We evaluated two cases: one at low altitude and a relatively low Mach number ($M=10$, $z=20$ km), and another with higher Mach and altitude values ($M=16$, $z=50$ km), both at zero angle of attack. Fig. 4, shows the electron number densities, plasma frequencies, and collision frequencies for the two different hypersonic flight conditions. These scenarios are related to the cone being studied, with a null angle of attack. The values shown represent the maximum values along the stagnation axis and at various vertical stations along the symmetry axis, which are indicated by red lines in the figure inset. It is observed that there are negligible differences in plasma properties between the conditions obtained using different ki-

netic parameters. Hence, we will exclusively present findings derived from Park's thermochemical model, which has been widely adopted in literature and can be used as a reference for readers who want to replicate or compare our results in their own research.

3.2. CFD results

In this section, we report on the numerical results obtained by considering a test matrix of different Mach/altitude pairs. These conditions were found to be relevant from the perspective of plasma properties and adequately cover at least part of a possible path of a gliding hypersonic vehicle. A visual representation of the conditions considered is shown in Fig. 5. The red dots indicate the simulated trajectory points. It is worth noting that in the red region, the Mach/altitude combinations would lead to excessively high temperatures at the nose wall, as we observed in some numerical experiments, and for this reason, we decided to discard that area from this study.

3.2.1. Roto-translational and vibrational-electron temperature

Fig. 6 displays the roto-translational temperature in the domain resulting from an axisymmetric flow field, and thus with a zero angle of attack. These simulations considered various Mach and altitude conditions which were revealed to be relevant from the perspective of plasma properties. As expected, the highest values of roto-translational temperature can be observed in the nose region, where the shock wave is most intense. It's worth noting that higher temperatures are obtained as the Mach number - responsible for greater heating and compression by the shock wave - increases. Regardless of the case, the wake shows temperatures on the order of thousands of Kelvin, making it an area of non-negligible thermochemical activity. On the other hand, Fig. 7 illustrates the outcomes related to the vibrational-electronic temperature under the same conditions. To ensure a major clarity of the results, the same scale of the roto-translational temperature has been used. Upon comparing Fig. 6 with Fig. 7, it's evident that a certain degree of thermal non-equilibrium is present in all the cases considered. This non-equilibrium is not only limited to the area downward the shock wave but extends throughout the wake region. The strong expansion experienced by the gas at the trailing edge of the cone provokes a decrease in the roto-translational energy, which is not accompanied by a vigorous decrease of the vibrational energy, as the latter remains frozen to values higher than those pertaining to local equilibrium. In those regions, the vibrational temperature is higher than the roto-translational temperature, making dissociation more efficient with respect to a model

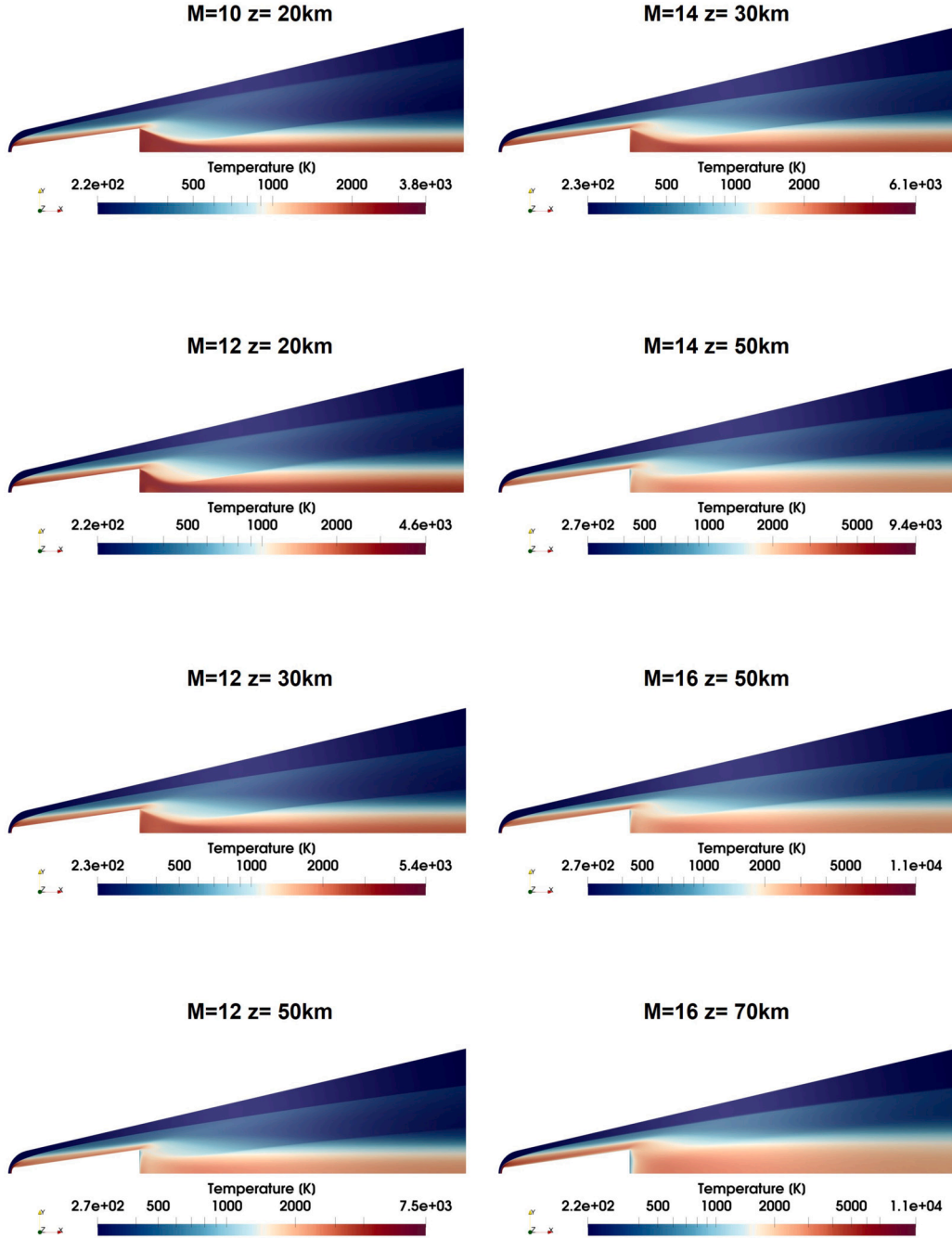


Fig. 6. Roto-translational temperature for various Mach numbers and altitude scenarios.

where internal energy equilibrium is assumed. Therefore, the presence of thermal non-equilibrium in the wake region emphasizes its significant influence on plasma properties, underscoring the importance of considering these mechanisms and this area when evaluating plasma characteristics.

3.2.2. Electron number density and plasma frequency

Fig. 8 illustrates the distribution of electron number density within the flow fields. The results highlight the substantial impact of ionization under the examined flight conditions. Notably, electron densities peak at the nose of the cone, from where electrons migrate towards the wake. With increasing Mach numbers, thermochemical activity intensifies, resulting in the heightened formation of charged species. In all depicted cases, electron density in the wake is non-negligible. It is espe-

cially significant to underline that in scenarios featuring Mach numbers of 12 at an altitude of 20 km, Mach 14 at 30 km altitude, and Mach 16 at 50 km altitude, the electron density in the wake exhibits remarkably elevated levels. The high electron number density in the flow field results in high values of plasma frequencies. Considering Fig. 9, it is evident that a layer surrounds the cone where the plasma frequencies are significant, corresponding to the electron density pattern. The plasma frequency near the body reaches GHz levels, whereas in the wake region, values around the MHz range can be observed. In some instances, such as $M=12$ and $z=20$ km and $M=14$ and $z=30$ km, the wake zone exhibits plasma frequencies up to GHz. As the altitude increases, relevant values of plasma frequency in the wake can be observed at a greater distance from the axis of symmetry, depicting a thicker layer of plasma in the wake [51].

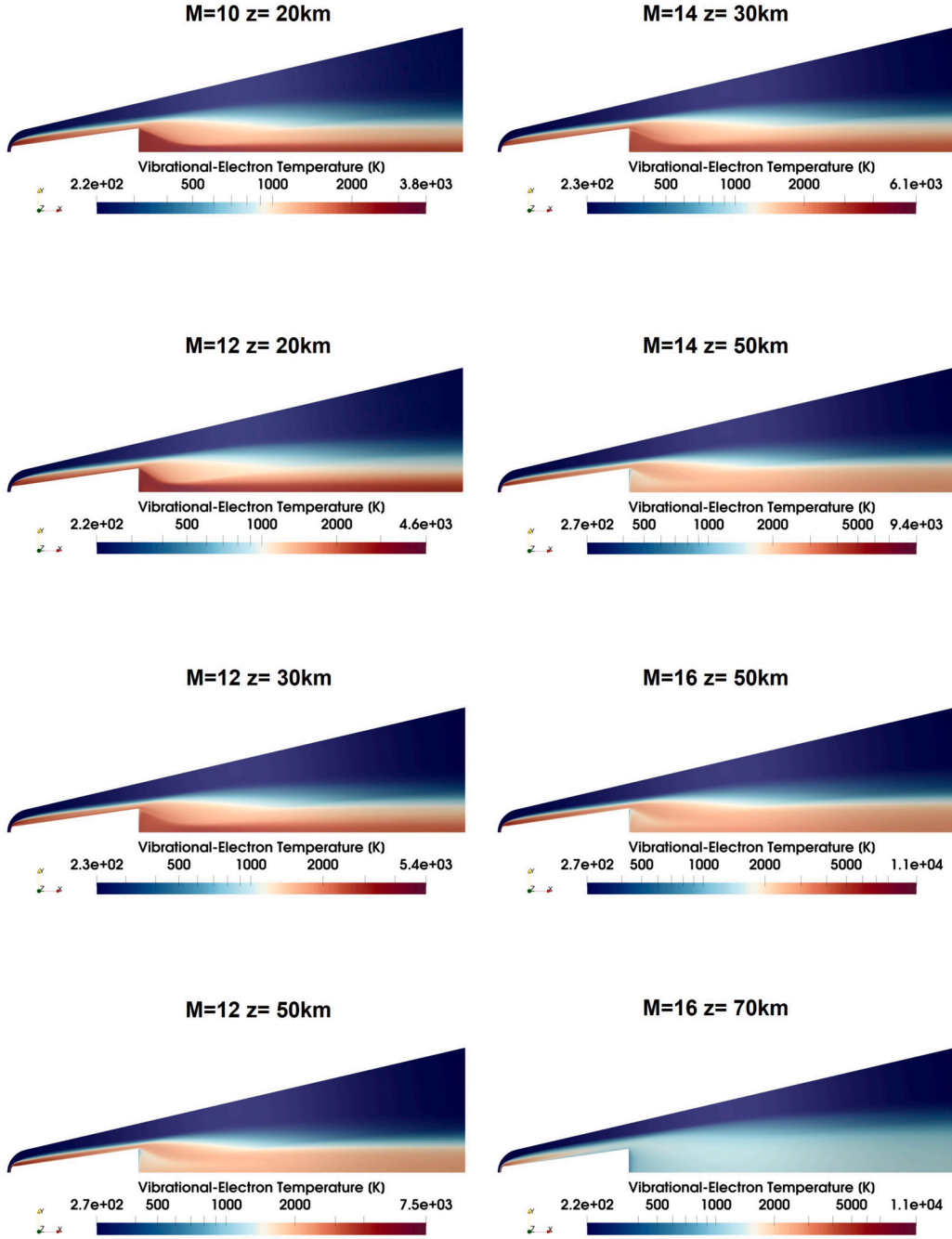


Fig. 7. Vibrational-electron temperature for various Mach numbers and altitude scenarios.

3.2.3. Collision frequency

Fig. 10 displays the collision frequency fields. The areas with the highest frequencies can be found around the cone where dissociation phenomena are more intense and temperatures are higher. The wake of the cone displays a pattern similar to temperature, with a very low collision frequency zone in the rear region. This latter is because of the expansion fan located at the trailing edge of the cone, which causes fluid expansion, lowering temperature and density. After analyzing various flight conditions, it is evident that lower altitudes (20 and 30 km) have significantly higher collision frequency values compared to higher altitudes. For instance, collision frequencies at an altitude of 20 km and a Mach number of 10 reach a peak of approximately 70 GHz. However, at an altitude of 70 km, even with a relevant Mach number of 16, the compression of the shock wave is not sufficient to observe significant collision frequencies, and the maximum value is approximately of 160

MHz at the nose. The main reason for this is the higher air density in the free stream conditions, which results in more significant dissociation downward of the shockwave and, consequently, a higher number density of neutral species. In this case, as the Mach number increases for a fixed altitude, collision frequencies also increase.

3.2.4. Dielectric constant

Due to the just observed flow field's characteristics, the dielectric constant exhibits strong inhomogeneity. Fig. 11 displays the real part of the dielectric constant at an EM wave frequency of 1 GHz. The choice of a 1 GHz EM frequency is an example related to practical applications in radar detection, radar guidance, and telecommunications [51]. In fact, many military radars operate in the L and S radar bands (1-4 GHz), as do GPS and some communication satellites. Fig. 11 shows that the nose of the cone has a region with negative permittivity in most

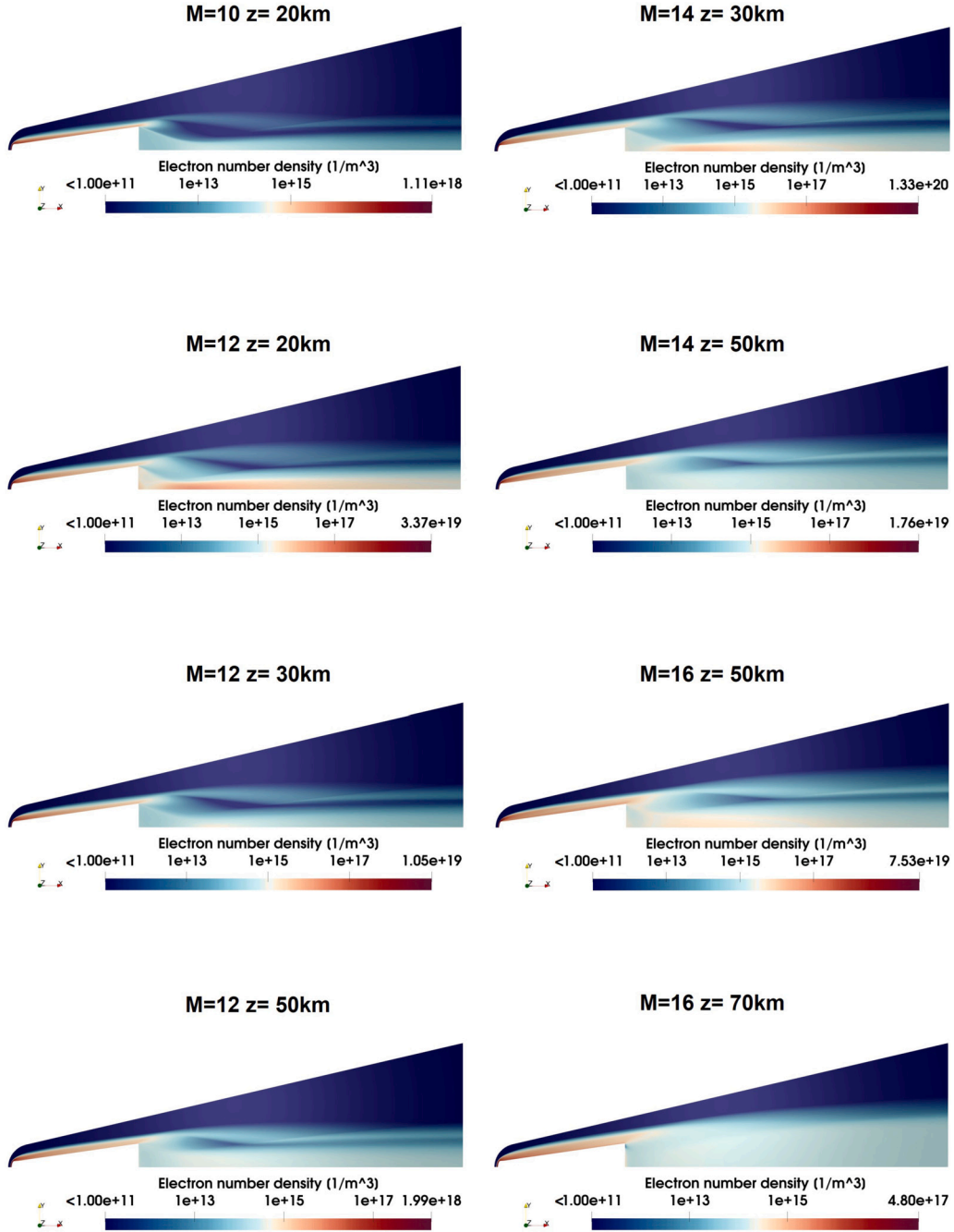


Fig. 8. Electron number density for various Mach numbers and altitude scenarios.

of the examined conditions. It's worth noting that the most significant cut-off condition occurs at $M=14$ and $z=30$ km, and $M=16$ and $z=50$ km, with negative permittivity values affecting almost the entire body. Examining the wake, it is observed that the conditions at $M=12$ and $z=20$ km, and $M=14$ and $z=30$ km, present a region with negative permittivity, forecasting EM wave reflection in that area. For the condition at $M=16$ and altitude $z=50$ km, a wake with positive but less than unity permittivity values is observed, forecasting a pronounced refractive area. At a flight condition of $M=10$ and $z=20$ km, there are no relevant values considering the real part of the permittivity. However, an analysis of the imaginary part of the dielectric constant in Fig. 12 reveals elevated values on the body, responsible for collisional absorption and EM wave attenuation. At low altitudes, such as 20 km, collisional absorption is more pronounced due to the greater presence of neutral species, resulting from the higher overall number density in free-stream

conditions, which leads to an increase in collision frequency. As the altitude increases, the effects of collisional absorption drastically decrease for the same reason. According to Eq. (3), these effects become more significant as the frequency of the EM wave decreases.

3.3. CFD results for a 3D case

In this section, we discuss a non-axisymmetric scenario, in which the body is inclined by an angle $\alpha = 6^\circ$ with respect to the direction of the free stream. The analyzed flight condition corresponds to a Mach number of 12 and an altitude of 20 km, which, as discussed in the previous section, proved significant in terms of both collisional absorption and cut-off in the wake of the cone. Upon analyzing Fig. 13, it is apparent that the plasma frequency values in the nose region closely resemble those at zero angle of attack. However, in the wake, the electron den-

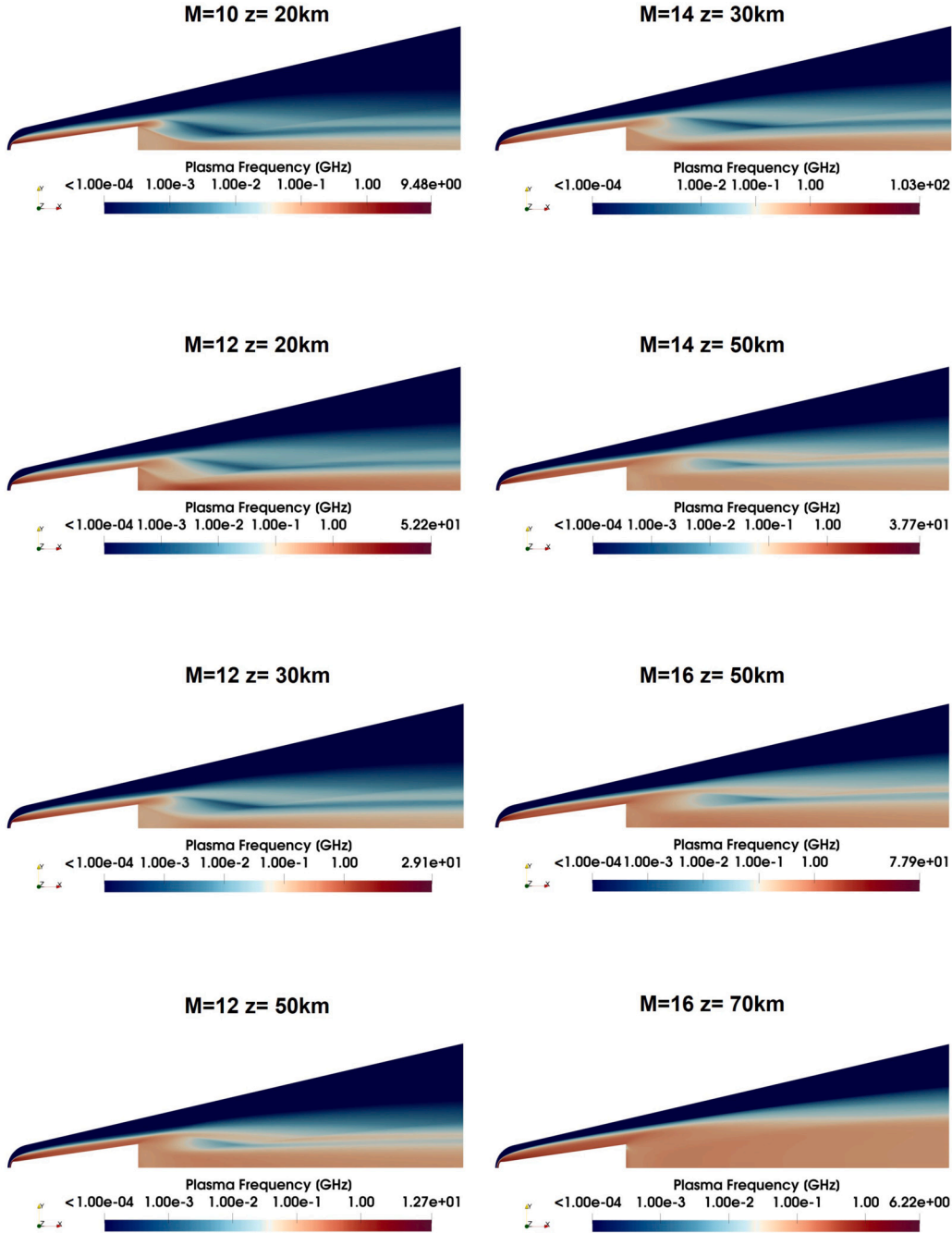


Fig. 9. Plasma frequency for various Mach numbers and altitude scenarios.

sities are much lower, causing the plasma frequencies to not reach the GHz levels observed in the axisymmetric scenario. This effect is mainly attributable to the expansion fan at the trailing edge, which is extremely intense on the windward side of the cone, strongly expanding the fluid and consequently reducing the electron density. Another effect is related to the asymmetry of the aft recirculation bubble, which presents a weaker reattachment shock wave in the case at $\alpha = 6^\circ$. All of these results in an asymmetric distribution of the plasma density in the wake, where higher plasma frequencies are reached (in the hundreds of MHz range) in the upper region compared to the lower one (in the tens of MHz range). In Fig. 14, collision frequencies ranging from MHz to GHz are observed in the wake. Specifically, the core of the wake downstream from the cone's rear displays very low frequencies (in the tens of MHz range) due to the expansion fans at the edges which make this area a low-density region. On the other hand, the outer part of the wake, which

contains a high concentration of neutral species, shows clearly visible GHz frequencies. Focusing on the core of the wake, from the rear of the cone toward the outflow, collision frequencies tend to increase, reaching values in the GHz range.

The real and imaginary components of the dielectric constant are reported in Fig. 15 and 16, respectively. These values were computed using an electromagnetic wave frequency of 1 GHz. Upon examining the real part of the dielectric constant in Fig. 15, we observe less significant values when compared to the axisymmetric case. Due to considerably lower plasma frequency values, negative permittivity values are not observed in the wake. However, a region of permittivity values less than one persists in the wake, forecasting refraction phenomena for the considered EM frequency. Consistent with the plasma frequency pattern, the refractive zone is confined to the upper part of the wake, where frequencies in the hundreds of MHz are reached. Regarding the imaginary

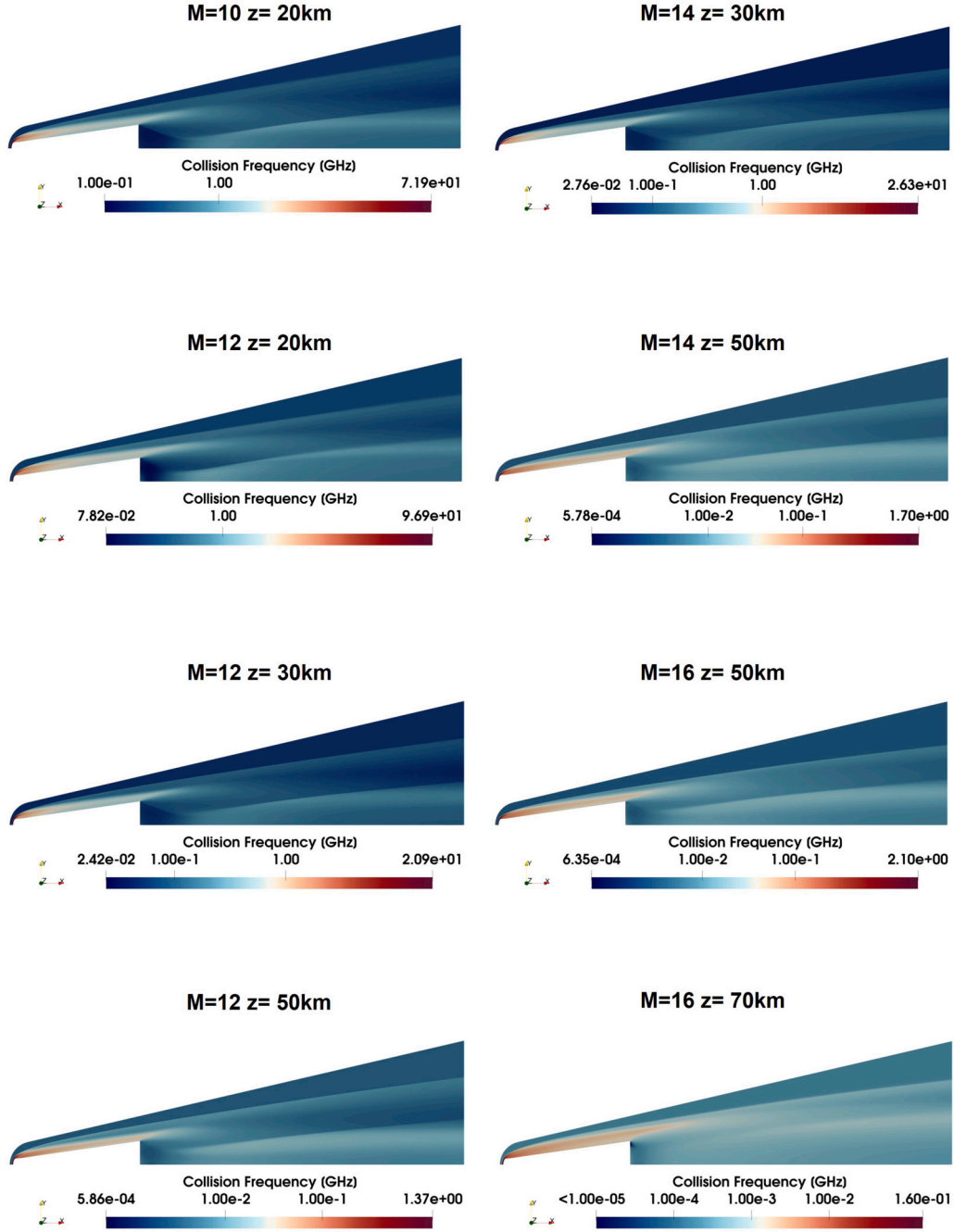


Fig. 10. Collision frequency for various Mach numbers and altitude scenarios.

part of the dielectric constant in Fig. 16, significant values are also observed over the nose and approximately half of the body, but much less in the wake compared to the axisymmetric case. Once again, we observe that the wake adheres to the pattern associated with the plasma frequency field. Here, values around 10^{-1} are observed, foreshadowing a much milder effect of collisional absorption compared to the axisymmetric case.

3.4. CEM results

To enhance comprehension of EM scattering and plasma influences, especially in the wake, we present computational electromagnetism (CEM) analysis for a scenario with Mach 14 and an altitude of 30 km. Fig. 17 displays the results of a Finite-Difference Time-Domain (FDTD)

analysis conducted at a frequency of 1 GHz and an incident angle of $\theta = -135^\circ$, assessing the bistatic RCS (BRCS) [52].

The commercial software CST Studio Suite was used for this investigation [53]. The figure illustrates the RCS as a function of the observation angle, and the inset provides a visualization of the observation setup, emphasizing the angle at which the EM wave strikes the cone. The black curve illustrates results for a vacuum environment, the red curve incorporates plasma effects around the cone and in the wake, while the blue curve represents plasma only in the body region, excluding the wake. These results suggest that plasma has a significant impact on the distribution of electromagnetic scattered fields, and therefore, bistatic RCS (BRCS) when compared to a vacuum environment. The RCS is redistributed across the entire angular spectrum, as observed immediately. Overall, it is observed that the presence of the wake leads to an increase in RCS in the forward scattering direction ($\theta = 45^\circ$) by about 7 dBsm

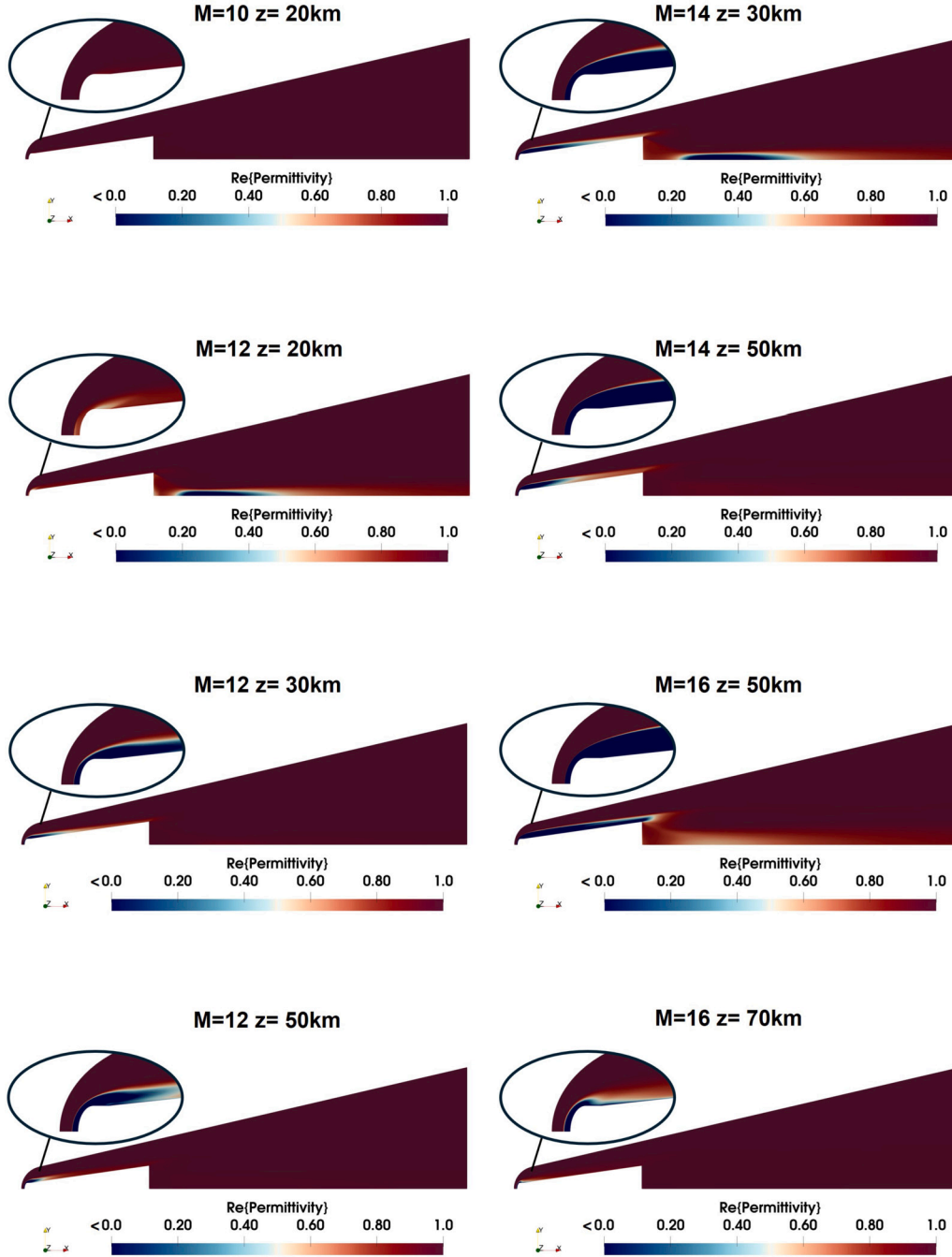


Fig. 11. Real part of dielectric constant for various Mach numbers and altitude scenarios considering an EM frequency of 1 GHz.

compared to vacuum and 3 dBsm compared to the wake-less plasma case. In the peak reflection direction ($\theta_{ref} = -54^\circ$), there is an increase in RCS with a maximum peak of 4 dBsm for the wake case compared to both wake-less and vacuum cases. The fully reflective (negative permittivity) plasma layer covers about the half of the body length but it is rather thin and the intensity of the reflected radiation by the body alone remains almost unchanged in this case (only a small increase of about 0.3 dB with plasma). Conversely, the wake changes the RCS not only near the θ_{ref} but in a wide angular range $0 < \theta < \theta_{ref}$ highlighting the strong refracting and reflecting effect of the plasma wake.

In the backscattering direction ($\theta = -135^\circ$), the RCS remains substantially unchanged for both plasma cases compared to the vacuum case.

The reliability and accuracy of the presented results require careful consideration, particularly due to the limited availability of experimen-

tal data under similar plasma conditions. While the computational analysis using CST Studio Suite provides valuable insights into the effects of plasma on electromagnetic scattering, full validation necessitates a systematic comparison with experimental measurements, which are scarce in both laboratory and aerospace environments. Additionally, the choice of frequency is a critical factor in determining the electromagnetic response for a given plasma condition. In fact, when the ratio between the electromagnetic and plasma frequencies approaches unity, significant changes in the RCS can occur with small variations in frequency. Outside this regime, changes are expected to be more gradual. Such sensitivity suggests that the results, while informative, should be interpreted with caution, particularly when considering different frequencies or plasma conditions not explicitly analyzed. A more comprehensive frequency-dependent analysis is necessary to fully assess the accuracy of the findings, which is not carried out here, as the central focus of this

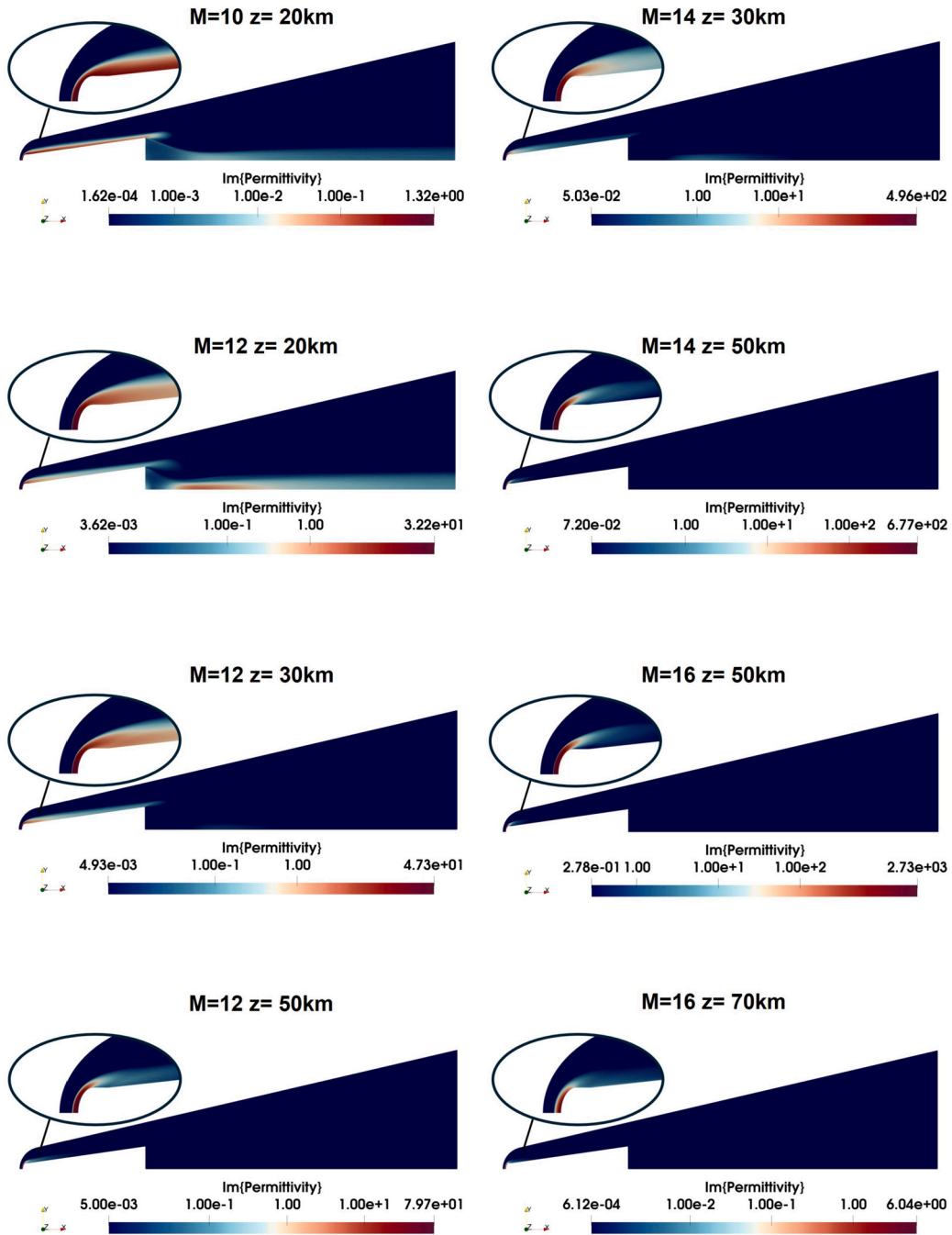


Fig. 12. Imaginary part of dielectric constant for various Mach numbers and altitude scenarios considering an EM frequency of 1 GHz.

paper is analyzing the non-equilibrium plasma distribution in the wake of a slender blunted-nose cone in hypersonic flight, with examples of its effects on the RCS.

The EM analysis of the other hypersonic cruise conditions shown in this work will be presented elsewhere, together with the comparison between different CEM numerical methods and radio frequencies.

4. Conclusions

This paper presents a comprehensive analysis of the flow field around and in the wake of a slender hypersonic cone under various flight conditions, emphasizing the importance of plasma presence in the wake. The study employs an aerothermodynamic model incorporating non-equilibrium relaxation for a seven-species gas mixture, with a focus on plasma distribution in the wake region. The thermochemical model used

in this research, employing the Park two-temperature reaction scheme, captures the non-equilibrium phenomena associated with hypersonic flight. Validation against experimental data demonstrates the model's ability to predict electron number densities consistent with observed trends, ensuring its reliability for hypersonic flow simulations. Results from the numerical simulations reveal significant plasma formation, particularly in the nose region of the slender body, with charged particles transported downstream along the vehicle and persisting in the wake.

In the paper, the effect of Mach number and altitude on different plasma properties relevant to EM wave propagation is described in detail. The key findings from the results can be summarized as follows.

Concerning the roto-translational temperature, it is highest at the vehicle nose and increases with Mach number, as expected. The effect of Mach number on the post-shock temperature outweighs the effect of the freestream temperature increase as altitude decreases, meaning the

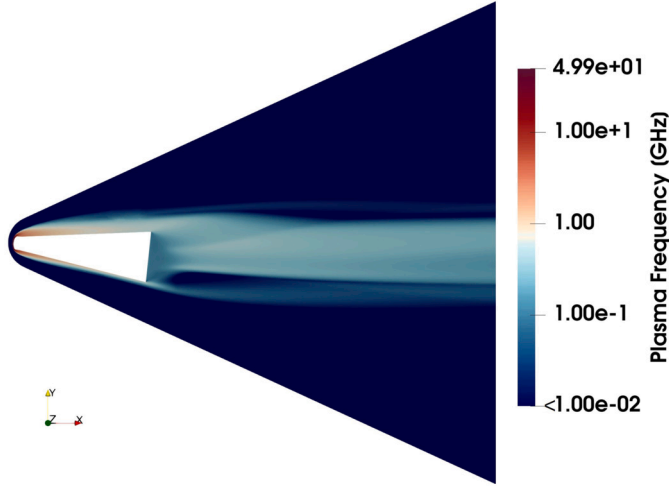


Fig. 13. Plasma frequency for Mach number $M = 12$ and altitude $z = 20$ km.

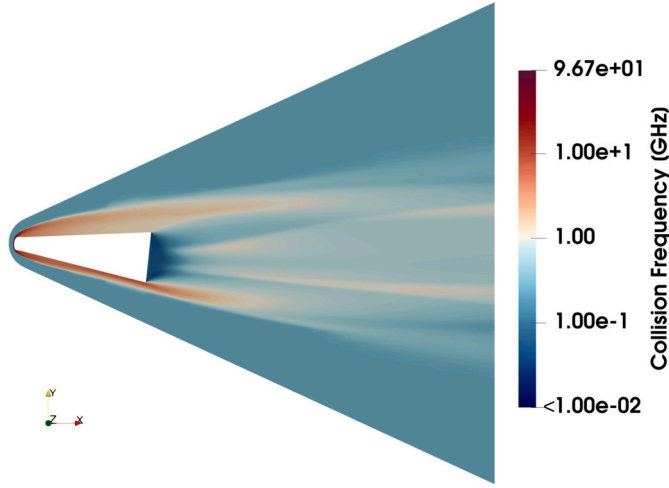


Fig. 14. Collision frequency for Mach number $M = 12$ and altitude $z = 20$ km.

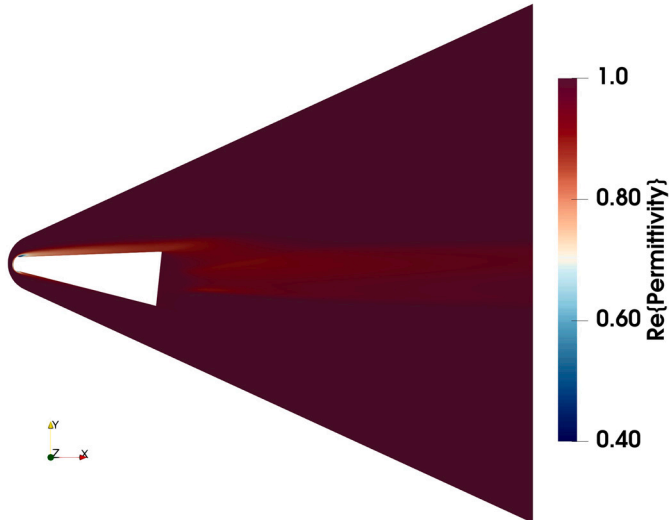


Fig. 15. Real part of the dielectric constant for Mach number $M = 12$, altitude $z = 20$ km and frequency of the EM wave $f = 1$ GHz.

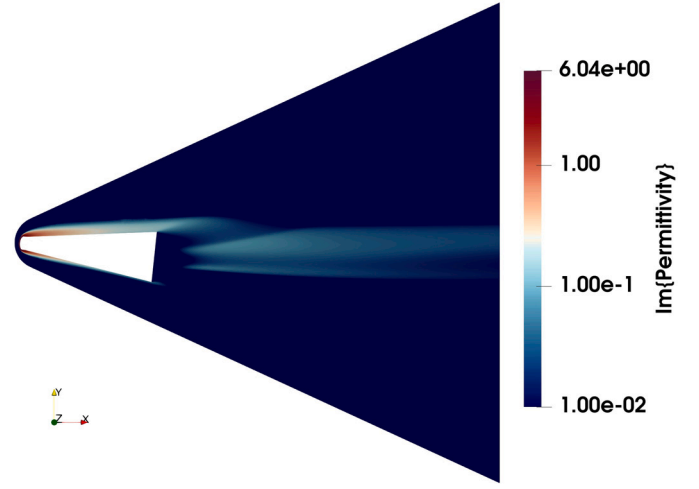


Fig. 16. Imaginary part of the dielectric constant for Mach number $M = 12$, altitude $z = 20$ km and frequency of the EM wave $f = 1$ GHz.

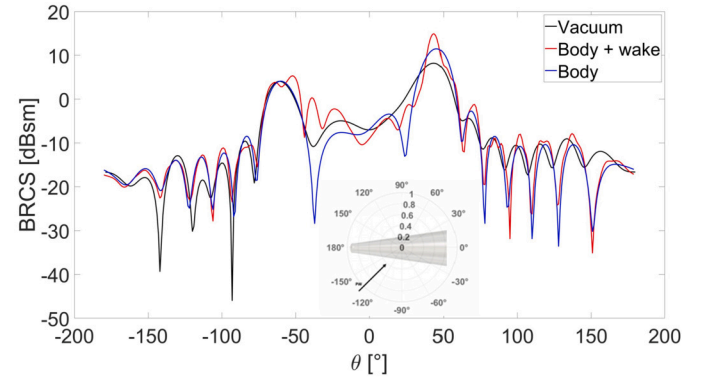


Fig. 17. Comparison of bistatic RCS with plasma in the wake and enveloping the cone (red line), plasma enveloping only the cone (blue line), and in a vacuum (black line). The flight condition refers to a Mach number of 14 and an altitude of 30 km.

highest temperatures are observed at the highest Mach numbers, while altitude is less significant. The vibrational-electronic temperature in the wake is clearly in a non-equilibrium state, likely due to the strong expansion the gas undergoes at the trailing edge of the body, leading to the freezing of that thermal degree of freedom. In some parts of the wake, this phenomenon affects the production and maintenance of charged species, as the decrease in roto-translational temperature caused by the strong expansion at the vehicle's tail is mitigated by the persistence of relatively high vibrational-electronic temperature.

Electron number density, and consequently plasma frequency, are highest around the vehicle nose due to the high temperature, which induces strong dissociation and ionization activity. The plasma generated at the nose is then convected around the vehicle, forming the so-called “plasma sheath”. The greatest amount of charged species and correspondingly high plasma frequency occur, for a given Mach number, at lower altitudes. Referring to the graph in Fig. 5, this corresponds to the lower boundary of our test case matrix. Plasma also persists in the wake. In some instances, recompression shocks in the wake are so intense that they produce a significant amount of charged species locally. This typically happens at the lowest boundary of the test matrix shown in Fig. 5. Generally, when the Mach number is sufficiently high, hypersonic flight tends to generate more charged species at lower altitudes than at higher altitudes.

Collision frequency is strongly influenced by altitude due to its dependence on gas number density. At low altitudes, where gas density is higher, collision frequency is always greater than at high altitudes. This

effect is so strong that it surpasses the intensity of the shock wave. Under fixed freestream conditions, collision frequency is higher near the nose due to the elevated temperature and related dissociation phenomena, which increase the number of gas particles and thus the number density. The strong expansion experienced by the gas in the wake significantly reduces gas density, resulting in lower collision frequency in that region.

Negative values of the real part of the dielectric constant (permittivity), which indicate cut-off conditions, are present around the nose of the cone under most considered conditions but involve a greater portion of the cone in the lower boundary of the considered test case matrix starting from Mach 14. Negative permittivity, and thus EM wave reflection, is also present in the wake at low altitudes (20–30 km) and relatively low Mach numbers (12–14). At low altitude (20 km) and even smaller Mach numbers (10), cut-off is not present, but collisional absorption - and thus EM wave attenuation - linked to high values of the imaginary part of the dielectric constant, is observed. Collisional absorption is typical at low altitudes due to the larger gas density and greater presence of neutral species.

The effect of the angle of attack reduces plasma presence in the wake for two reasons. First, the flow expands more strongly at the tail than at zero incidence, decreasing the temperature and promoting gas neutralization. Second, the wake asymmetry reduces the intensity of reattachment shocks, which contribute less to local electron production in the wake.

The final EM wave analyses, incorporating plasma effects, illustrate the alteration of the RCS due to the presence of the plasma. The results of the FDTD simulations highlight the contribution of the plasma wake to the RCS redistribution. Overall, this study underscores the critical role of wake plasma in affecting the scattering of EM waves and the radar signature of aircraft. Future works will include expanding the RCS analysis to cover additional flight conditions and considering different frequencies and angles of incidence for the EM wave. Further investigations will focus on quantifying the effect of collisional absorption.

CRediT authorship contribution statement

Salvatore Esposito: Writing – review & editing, Writing – original draft, Visualization, Validation, Investigation, Formal analysis, Data curation, Conceptualization. **Andrea Scarabosio:** Writing – review & editing, Writing – original draft, Supervision, Formal analysis. **Giuseppe Vecchi:** Writing – review & editing, Supervision, Formal analysis. **Domenic D'Ambrosio:** Writing – review & editing, Writing – original draft, Supervision, Investigation, Formal analysis.

Declaration of competing interest

The authors declare that they have no known competing financial interests or personal relationships that could have appeared to influence the work reported in this paper.

Acknowledgements

The doctoral scholarship that supported this research was funded under Ministerial Decree No. 1061 within the framework of the PON (Programmi Operativi Nazionali) “Research and Innovation” 2014–2020. We are grateful to the Italian Ministry of Education, University and Research (MIUR) for managing the PON funding program and for supporting our research endeavors.

Data availability

No data was used for the research described in the article.

References

- [1] J.D. Anderson, *Hypersonic and High Temperature Gas Dynamics*, 3rd ed., American Institute of Aeronautics & Astronautics, Reston, VA, 2019.
- [2] T.H. Stix, *Waves in Plasmas*, American Institute of Physics, Melville, NY, 1992.
- [3] N. Blaunstein, E. Plohotniuc, *Ionosphere and Applied Aspects of Radio Communication and Radar*, CRC Press, 2008.
- [4] K.G. Budden, *Radio Waves in the Ionosphere*, Cambridge University Press, 2009.
- [5] H. Singh, S. Antony, R.M. Jha, *Plasma-Based Radar Cross Section Reduction*, Springer, 2016.
- [6] G.V. Candler, Rate-dependent energetic processes in hypersonic flows, *Prog. Aerosp. Sci.* 72 (2015) 37–48.
- [7] G.V. Candler, Rate effects in hypersonic flows, *Annu. Rev. Fluid Mech.* 51 (2019) 379–402.
- [8] P.A. Gnoffo, Planetary-entry gas dynamics, *Annu. Rev. Fluid Mech.* 31 (1999) 459–494.
- [9] E. Nagnibeda, E. Kustova, *Non-equilibrium Reacting Gas Flows: Kinetic Theory of Transport and Relaxation Processes*, Springer Science & Business Media, 2009.
- [10] A.J. Eggers Jr, H. Ashley, G.S. Springer, J.V. Bowles, M.D. Ardema, Hypersonic waverider configurations from the 1950's to the 1990's, in: *International Hypersonic Waverider Symposium*, College Park, MD, 1990.
- [11] K. Kontogiannis, A. Söbester, N.J. Taylor, On the conceptual design of waverider forebody geometries, in: *53rd AIAA Aerospace Sciences Meeting*, 2015, AIAA-2015-1009.
- [12] V. Carandente, G. Zuppari, R. Savino, Aerothermodynamic and stability analyses of a deployable re-entry capsule, *Acta Astronaut.* 93 (2014) 291–303.
- [13] S. Kumar, S.P. Mahulikar, Aero-thermal analysis of lifting body configurations in hypersonic flow, *Acta Astronaut.* 126 (2016) 382–394.
- [14] G. Zuppari, R. Savino, G. Mongelluzzo, Aero-thermo-dynamic analysis of a low ballistic coefficient deployable capsule in Earth re-entry, *Acta Astronaut.* 127 (2016) 593–602.
- [15] A. Schettino, G. Pezzella, M. Marini, S. Di Benedetto, V.F. Villace, J. Steelant, R. Choudhury, A. Gubanov, N. Voevodenko, Aerodynamic database of the Hexafly-INT hypersonic glider, *CEAS Space J.* 12 (2020) 295–311.
- [16] D. Mather, J. Pasqual, J. Silience, P. Lewis, Radio frequency (RF) blackout during hypersonic reentry, in: *AIAA/CIRA 13th International Space Planes and Hypersonics Systems and Technologies Conference*, 2005, AIAA-2005-3443.
- [17] S. Ramjatan, T. Magin, T. Scholz, V. Van der Haegen, J. Thoemel, Blackout analysis of small cone-shaped reentry vehicles, *J. Thermophys. Heat Transf.* 31 (2017) 269–282.
- [18] Y. Takahashi, K. Yamada, T. Abe, Prediction performance of blackout and plasma attenuation in atmospheric reentry demonstrator mission, *J. Spacecr. Rockets* 51 (2014) 1954–1964.
- [19] Z. Cong, Z. He, R. Chen, An efficient volumetric sbr method for electromagnetic scattering from in-homogeneous plasma sheath, *IEEE Access* 7 (2019) 90162–90170.
- [20] A. Scarabosio, J.L.A. Quijano, J. Tobon, M. Righero, G. Giordanengo, D. D'Ambrosio, L. Walpot, G. Vecchi, Radiation and scattering of em waves in large plasmas around objects in hypersonic flight, *IEEE Trans. Antennas Propag.* 70 (2022) 4738–4751.
- [21] J.-W. Qian, H.-L. Zhang, M.-Y. Xia, et al., Modelling of electromagnetic scattering by a hypersonic cone-like body in near space, *Int. J. Antennas Propag.* 2017 (2017) 3049532.
- [22] J. Tong, H. Li, B. Xu, S. Wu, L. Bai, Excitation and power spectrum analysis of electromagnetic radiation for the plasma wake of reentry vehicles, *Plasma Sci. Technol.* 25 (2023) 055301, <https://doi.org/10.1088/2058-6272/aca7ad>.
- [23] W.L. Jones, A.E. Cross, Electrostatic-probe measurements of plasma parameters for two reentry flight experiments at 25000 feet per second, *National Aeronautics and Space Administration*, 1972, NASA TN D-6617.
- [24] Y.-X. Sha, H.-L. Zhang, X. Guo, M. Xia, Analyses of electromagnetic properties of a hypersonic object with plasma sheath, *IEEE Trans. Antennas Propag.* 67 (2019) 2470–2481.
- [25] G. Niu, Y. Liu, B. Bai, Y. Ding, L. Song, X. Li, Polarization scattering characteristic of plasma-sheath-covered hypersonic vehicle, *IEEE Trans. Plasma Sci.* 51 (2023) 641–648.
- [26] W.F. Chen, W.W. Zhao, *Rarefied Gas Dynamic Moment Method and Numerical Simulation*, Science Press, Beijing, China, 2017.
- [27] Z. Bian, J. Li, L. Guo, Simulation and feature extraction of the dynamic electromagnetic scattering of a hypersonic vehicle covered with plasma sheath, *Remote Sens.* 12 (2020) 2740, <https://doi.org/10.3390/rs12172740>.
- [28] Z. Bian, J. Li, L. Guo, X. Luo, Analyzing the electromagnetic scattering characteristics of a hypersonic vehicle based on the inhomogeneity zonal medium model, *IEEE Trans. Antennas Propag.* 69 (2021) 971–982, <https://api.semanticscholar.org/CorpusID:226435504>.
- [29] Z. Bian, J. Li, L. Guo, ISAR imaging analysis of a hypersonic vehicle covered with plasma sheath, *IEEE Trans. Geosci. Remote Sens.* 60 (2022) 2002413.
- [30] Y.-G. Lv, L.-X. Guo, J.-T. Li, *Hypersonic Vehicle Plasma Sheath and Electromagnetic Characteristics Data Manual*, Science Press, 2019.
- [31] H. Zhang, J. Li, C. Qiu, Z. Yu, Z. Bian, L. Guo, L. Guo, S. Liu, Electromagnetic scattering characteristics of a hypersonic vehicle with a microrough surface in the millimeter wave band, *AIP Adv.* 13 (2023) 095215, <https://doi.org/10.1063/5.0160916>.
- [32] Y. Wang, S. Liu, S. Zhong, Studies on the effects of the plasma wake flow fields of hypersonic reentry blunt cone on electromagnetic wave, *IEEE Trans. Plasma Sci.* 47 (2019) 3991–3996, <https://doi.org/10.1109/TPS.2019.2926166>.

- [33] C. Shao, L. Nie, W. Chen, Analysis of weakly ionized ablation plasma flows for a hypersonic vehicle, *Aerosp. Sci. Technol.* 51 (2016) 151–161.
- [34] C. Park, Assessment of two-temperature kinetic model for ionizing air, *J. Thermophys. Heat Transf.* 3 (1989) 233–244.
- [35] C. Park, Calculation of nonequilibrium radiation in the flight regimes of aeroassisted orbital transfer vehicles, in: *AIAA 22nd Aerospace Science Meeting*, 1984, AIAA-84-0306.
- [36] C. Park, Problems of rate chemistry in the flight regimes of aeroassisted orbital transfer vehicles, in: *AIAA 19th Thermophysics Conference*, 1984, AIAA-94-1730.
- [37] P.A. Gnoffo, Conservation equations and physical models for hypersonic air flows in thermal and chemical nonequilibrium, NASA-TP-2867, NASA, 1989.
- [38] R.N. Gupta, J.M. Yos, R.A. Thompson, K.-P. Lee, A review of reaction rates and thermodynamic and transport properties for an 11-species air model for chemical and thermal nonequilibrium calculations to 30000 K, NASA-RP-1232, NASA, 1990.
- [39] C. Park, Review of chemical-kinetic problems of future NASA missions. i-earth entries, *J. Thermophys. Heat Transf.* 7 (1993) 385–398.
- [40] C. Park, R.L. Jaffe, H. Partridge, Chemical-kinetic parameters of hyperbolic Earth entry, *J. Thermophys. Heat Transf.* 15 (2001) 76–90.
- [41] J.G. Kim, S.M. Jo, Modification of chemical-kinetic parameters for 11-air species in re-entry flows, *Int. J. Heat Mass Transf.* 169 (2021) 120950.
- [42] R. Petervari, A. Nekris, T. Bieker, Numerical analysis of radar-plasma-signatures of a sphere in a Mach 10 hypersonic wind tunnel flow, in: *2021 18th European Radar Conference (EuRAD)*, 2022, pp. 86–89.
- [43] P. Drude, Zur Elektronentheorie der Metalle, *Ann. Phys.* 306 (1900) 566–613.
- [44] L.D. Landau, E.M. Lifshits, L.P. Pitaevskii, *Statistical Physics*, vol. 5, third ed., Butterworth-Heinemann, 1980.
- [45] S. Chakravarthy, O. Perroomian, U. Goldberg, S. Palaniswamy, The CFD++ computational fluid dynamics software suite, in: *AIAA and SAE, 1998 World Aviation Conference*, 1998, AIAA-1998-5564.
- [46] O. Perroomian, S. Chakravarthy, S. Palaniswamy, U. Goldberg, Convergence acceleration for unified-grid formulation using preconditioned implicit relaxation, in: *36th AIAA Aerospace Sciences Meeting and Exhibit*, 1998, AIAA-1998-116.
- [47] F.R. Menter, Improved two-equation k-omega turbulence models for aerodynamic flows, NASA-TM-103975, NASA, 1992.
- [48] L.J. Sullivan, The early history of reentry physics research at Lincoln Laboratory, *Linc. Lab. J.* 4 (1991) 113–132.
- [49] G.F. Pippert, On the structure of wake turbulence deduced from field radar measurements, in: *Conference on Physics of Entry into Planetary Atmospheres*, Cambridge, MA, USA, 1963, AIAA-1963-446.
- [50] P.A. Gnoffo, C.O. Johnston, R.A. Thompson, Implementation of radiation, ablation, and free energy minimization in hypersonic simulations, *J. Spacecr. Rockets* 47 (2010) 251–257.
- [51] M.I. Skolnik, *Radar Handbook*, third ed., McGraw & Hill, 2008.
- [52] J.-M. Jin, *Theory and Computation of Electromagnetic Fields*, John Wiley & Sons, 2015.
- [53] CST Studio Suite 2019, Dassault Systèmes, 2019.